International Journal of Heat and Mass Transfer 52 (2009) 5113–5121

Contents lists available at ScienceDirect

International Journal of Heat and Mass Transfer

journal homepage: www.elsevier.com/locate/ijhmt

Experimental study of biporous wicks for high heat flux applications

Tadej Semenic *, Ivan Catton

Department of Mechanical and Aerospace Engineering, University of California, Los Angeles, 46-147N Engineering IV, 420 Westwood Plaza, Los Angeles, CA 90095-1597, United States

ARTICLE INFO

Article history:
Received 3 June 2008
Received in revised form 16 April 2009
Available online 13 June 2009

Keywords:
Biporous wick
Electronics cooling
Heat pipe wick
High heat fluxes
Monoporous wick

ABSTRACT

Biporous wicks are wicks with two distinguished characteristic pore sizes while monoporous wicks are wicks with a single characteristic pore size. In this work three monoporous and 19 biporous wicks were tested. Thermophysical properties for the biporous wicks were measured.

Thin biporous wicks distinguish from thick biporous wick by mechanism of heat transfer that occurs inside the wick. Thin biporous wicks remove heat similar to monoporous wicks by evaporation from menisci formed inside pores at liquid–vapor–solid interfaces. Thin biporous wicks were found to reach higher critical heat flux (CHF) than monoporous wicks because they develop evaporating menisci not only on top surface of the wick but also inside the wick. Thick biporous wicks were found to reach even higher CHF than thin biporous wicks because they continue to operate although the vapor blanket (film boiling) exists on the heated surface. This is possible because the top layer of the wick continues to supply liquid to the evaporating menisci above the vapor blanket region and vapor jets form between large pores of the wick and vent the vapor out of the wick. It was also found that for thick biporous wicks operating at very high heat fluxes, the heat conducts radially into the wick.

The best monoporous wick tested had CHF at 300 W/cm^2 (21 °C superheat), the best thin biporous wick tested had CHF at 520 W/cm^2 (50 °C superheat), and the best thick biporous wick tested had CHF at 990 W/cm^2 (147 °C superheat). Thick biporous wicks can be used for 600–1000 W/cm^2 applications where high superheats and heat spreading into the wick are acceptable. For applications below 600 W/cm^2 are recommended thin biporous wicks and for applications below 300 W/cm^2 are recommended monoporous wicks.

1. Introduction

The development of contemporary high technology systems demands high performance heat transfer devices in order to accommodate increased rates of energy dissipation within these systems. Such heat transfer devices are required to avoid thermal damage due to high temperatures or temperature fluctuations. A passive thermal device that can very effectively dissipate a great deal of excess heat is a heat pipe. A highly isothermal character of heat pipe evaporators has led to their wide use in electronic cooling and other applications where an isothermal heat rejection surface is desired. Furthermore, heat pipes can be made in very small sizes and can very easily be implemented into an electronic device. The heat fluxes for an average heat pipe range from several tens to hundreds of watts per square centimeter and are limited by a heat transfer crisis occurring in the evaporator. Further, the condenser region of the heat pipe can be much larger than the evaporator making them very effective heat spreaders. The evaporator is very critical element of the heat pipe and is the focus of this work.

The evaporator is a solid interface between the device that is being cooled and the working fluid. It has three main functions: (1) it conducts heat from the device that is being cooled to the evaporating surface, (2) it supplies working fluid to the evaporating menisci by a capillary action, and (3) it allows the produced vapor to escape. A high heat flux evaporator is made of a heat conductive material with high capillarity, high liquid permeability, and high vapor permeability. This is difficult for evaporators with a single characteristic pore size (monoporous wicks) because the small pores needed for high capillary suction trap vapor within the evaporator. The vapor pockets block the fluid and prevent rewetting. A local dryout starts to form and then spreads to the entire evaporator.

A good compromise between high capillary pressure and high vapor permeability is found in biporous wicks where there are two separate and distinct pore size distributions. There are two types of biporous wicks: the first type are made of clusters of small particles, and the second are made of large rough particles with small pores on the surface. Fig. 1 shows a scanning electron microscope (SEM) micrograph of the first kind of the biporous wicks used in our study (cluster size 586 μm and particle size 74 μm or abbreviated 586/74). Several small pores can be seen between the copper particles, large pores are seen between the clusters.

* Corresponding author. Tel.: +1 310 825 5320; fax: +1 310 206 4830.
E-mail address: tadejsemenic@gmail.com (T. Semenic).

0017-9310/$ - see front matter © 2009 Elsevier Ltd. All rights reserved.
doi:10.1016/j.ijheatmasstransfer.2009.05.005

Nomenclature

a	value of a quantity
A	area (m^2)
B	bias uncertainty
d	particle diameter (μm), diameter (m)
D	cluster diameter (μm)
k	thermal conductivity (W/m K)
K	permeability (m^2)
p	pressure (Pa, bar)
P	precision uncertainty
R	thermal resistance per unit area (°C/W/cm^2)
q	heat flux (W/cm^2)
Q	heat (W)
S	standard deviation
T, t	temperature (°C), Student's t-distribution variable, thickness (μm)
U	uncertainty

Greek symbols

ε	porosity
μ	population mean
ζ	calculated temperature (°C)

Subscripts

$\bar{a}$	population mean
ave	average
c	center
e	evaporator
eff	effective
rad	radial
s	side
sat	saturated
T	temperature
x	position
w	wall, wick
1, 2	locations

The two pore sizes allow the biporous wicks to yield improved performance through separation of liquid and vapor phases.

During the operation of a biporous wick at high heat fluxes, the liquid phase is pumped through small pores of clusters by capillary action developed at the liquid/vapor menisci located on the surfaces of clusters. The vapor leaves the evaporator through the large pores.

Authors [1–5] compared performances of biporous wicks with monoporous wicks at high heat fluxes and they concluded that biporous wicks perform better. Rosenfeld and North [6] were able to reach a heat flux of 150 W/cm^2 using 9 cm^2 large biporous wick evaporator. Merilo et al. [7] made and tested a biporous wick that was able to handle a local heat fluxes of 310 W/cm^2 at a superheat of 18 °C. Semenic et al. [8] removed 495 W/cm^2 at 130 °C superheat using a thick biporous wick with an evaporator area of 0.7 cm^2. North [9] used biporous powder covered post arrays with the aid of screen arteries in the evaporator and was able to remove 930 W/cm^2 locally at superheat of 85 °C and 600 W/cm^2 at 55 °C superheat for the second run. Although preliminary knowledge about fluid flow and vaporization heat transfer in biporous wicks is available, it is far from being well understood and implemented in commercial heat pipes. An optimal biporous evaporator is able to reach a very high heat flux at low superheat. The objective of this work is to study different biporous wicks and to find a wick that is capable of removing 1 kW/cm^2 at low to intermediate superheat. The approach of the work is to:

- manufacture copper biporous wicks with different particle and cluster diameters, wick thickness, and evaporator areas,
- measure thermophysical properties of the wicks,
- test the wicks at different heat fluxes using water as working fluid, and
- find a wick with optimal wick geometry capable of removing 1 kW/cm^2 at low to intermediate superheat.

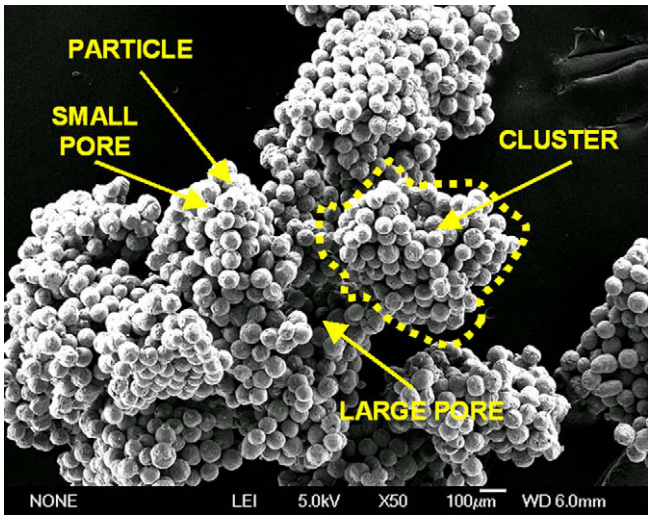

Fig. 1. SEM photograph of 586/74 biporous wick (magnification 50-times).

2. Thermo-hydraulics of monoporous and biporous wicks

Hanlon and Ma [10] developed a model for predicting heat transfer capability of a monoporous wick. The model is valid for the case where the fluid level is not above the top of the wick. The heat applied to the evaporator conducts through the evaporator wall and saturated wick made of sintered particles and passes through a thin film region that consists of three regions: the nonevaporating thin film region, the evaporation thin-film region, and the meniscus thin film region. The evaporation occurs in the thin film region on top surface of the wick where the liquid–vapor–solid interface exists. Thin film evaporation at the solid–liquid–vapor interface decreases dramatically when the fluid temperature inside the wick becomes superheated and bubble nucleation starts (boiling limit of the wick). The vapor generated at the base of the wick forms a blanket, increases wick thermal resistance and prevents re-entry of the wetting fluid. The film evaporation can also be interrupted if the capillary flow in the wick is interrupted due to insufficient capillary pumping (capillary limit of the wick). Capillary pumping is determined by effective capillary radius of the wick and wick permeability (wetting fluid flow resistance). Thin film evaporation can provide significantly higher overall heat transfer coefficients than boiling heat transfer, but it is limited by the capillary force and by the onset of bubble nucleation. Hanlon

and Ma [10] pointed out that high heat flux wicks should have the geometric parameters optimized to maximize thin film evaporation at the top surface of the wick. At the same time, the wick thermal resistance has to be minimized by minimizing wick thickness and by maximizing thermal conductivity of the wick. Thin wicks can have very low thermal resistance, but have, on the other hand, very high liquid flow resistance.

Rosenfeld and North [6] proposed a thermo-hydraulic model of a biporous wick. They argued that at low heat fluxes, the large pores of a biporous wick are filled with the working fluid and heat is removed from the wick by conduction through the saturated wick and evaporation from the top of the wick. At higher heat fluxes, the large pores become filled with vapor and the liquid is returned to the evaporator wick through the small pores within the clusters. The liquid is evaporated from the surface of the liquid saturated clusters in the interior of the wick. The produced vapor is vented out of the wick through large pores between clusters. At very high heat fluxes, the capillary pressure developed at the menisci of the small pores is insufficient to drive the liquid and the dryout of clusters begins.

Wang and Catton [11] proposed a physical model for vaporization in thick biporous wicks. The heat transfer mechanism within a thick biporous wick was divided into four stages:

First evaporation stage: at low heat fluxes, heat is conducted through the wick and evaporation occurs on the top of the wick. Evaporating menisci exist in small and large pores of the biporous wick. Heat transfer performance is worse than for a comparable monoporous wick due to much lower effective thermal conductivity of the biporous wick.

Heat pipe effect stage: when the heat flux is increased, the superheat at some portion of the wick is high enough to initiate nucleation. The growing bubbles start merging into vapor columns. Temperature decreases as one move from the heating surface toward the top of the wick, therefore, bubbles formed at the heated surfaces condense inside the wick and the vapor channels act as little heat pipes. The thermal capillary force difference between the lower and the upper region of the vapor column causes the liquid to circulate leading to very high effective thermal conductivity.

Boiling stage: with increasing heat flux, the pressure inside the vapor columns increase and in some columns it is high enough so that the vapor reaches the top of the wick. Some vapor columns remain active and some gets flooded with the liquid and the above process repeats.

Second evaporation stage: vapor escapes from the wick and the evaporating surface increases leading to an almost isothermal heat flux increase. Liquid is sucked inside the small pores. Heat is conducted through the liquid saturated clusters and is taken away by evaporation from the liquid–vapor interfaces in small pores.

Vapor blanket formation near the wall: near the wall the boiling is the most intensive and vapor blanket starts to form inhibiting downflow of the liquid. The vapor blanket grows and the dryout starts to spread.

Wang and Catton [11] also suggested a model of vaporization in thin biporous wicks. In the thin biporous wicks, at low heat flux, the heat is removed by conduction and evaporation. At moderate heat flux, the menisci in large pores recede resulting that many small pore menisci start to interface the vapor space and become active. At high heat flux, all the liquid is sucked into small pores and all large pores are clear of liquid. A thin vapor blanket may form on the heated surface at high heat fluxes and may result in a dryout of the wick. Wang and Catton [11] explained that a thin biporous media model is to be used if the wick is thin enough so that the bubble nucleation does not occur and the menisci recede into the large pores. A thick biporous wick, on the other hand is a wick where bubbles start to form inside the wick and to form vapor jets.

This work tested three monoporous and 19 biporous wicks. Biporous wicks had different particle diameters, cluster diameters, and wick thicknesses. Thermophysical properties such as porosity, capillarity, permeability, and thermal conductivity were measured for all biporous wicks tested. An optimal biporous wick is expected to have high liquid permeability through the clusters, high thermal conductivity, high capillary potential, and high vapor permeability through the large pores between the clusters. It is also expected that a thick biporous wick will transport more liquid and be able to reach higher critical heat flux (CHF), however, the critical superheat for the thick biporous wick is expected to be very high as well.

3. Experimental method

Raw spherical copper powder produced by high-pressure water atomization was sieved with standard US sieves into the following fractions: 32–45 μm (−325/+450), 53–63 μm (−230/+270), 63–75 μm (−200/+230), 63–90 μm (−170/+230), 75–90 μm (−170/+200), and 90–106 μm (−140/+170). Different fractions of powders were sintered into thin monoporous layers and ground into clusters. Produced clusters were sieved into fractions: 250–355 μm (−45/+60), 500–710 μm (−25/+35), and 710–1000 μm (−18/+25). Clusters were sintered on smooth oxygen free copper bases for wick performance tests. Samples with the same cluster (particle) diameter were sintered at the same sintering conditions. All the samples were manufactured by Advanced Cooling Technologies, Inc.

From the theory of sintering it is known that the pore size, smoothness and interconnectivity of the pores depend strongly on particle diameter and variance, material properties, temperature, and sintering time. With proper sintering, optimal bonding between particles is achieved and results in many small size, fully connected pores, with acceptable strength. Since we were dealing with particles with a size distribution, sintering diagrams could only be used as guidance. Furthermore, some materials such as copper do not sinter by a single independent mechanism. Consequently, inclusion of multiple effects adds to the errors in calculations and the overall sintering rates had to be determined experimentally. A scanning electron microscope (SEM) was used to monitor all stages of wick production and to determine proper overall sintering rates for particle sizes of interest. The most optimal particle neck size ratio was found to be around 0.4. Particle necks are welds or bonds between particles and the neck size ratio is defined as a neck dimension divided by the particle diameter.

The test wicks were sintered on the copper bases shown in Fig. 2. The heat source area was equal to the neck cross-section area of the copper base. The purpose of the wick sintered around the heat source (sintered on the collar of the copper base) was to supply the working fluid to the evaporator and to avoid side venting of the vapor. The wick material on the collar of the copper base assured that the vapor flow through a thick biporous wicks was in direction from the heat source to the top of the wick and not sideways where it could block the liquid supply to the evaporator wick (above the neck).

A copper base with a porous wick was sealed to the test rig (Fig. 3) with a silicone o-ring and six brass screws. The body of the test rig was made of Oxygen free copper. The heater consisted of a copper block with three 750 W cartridge heaters that were connected to a stepper motor controlled variable power supply.

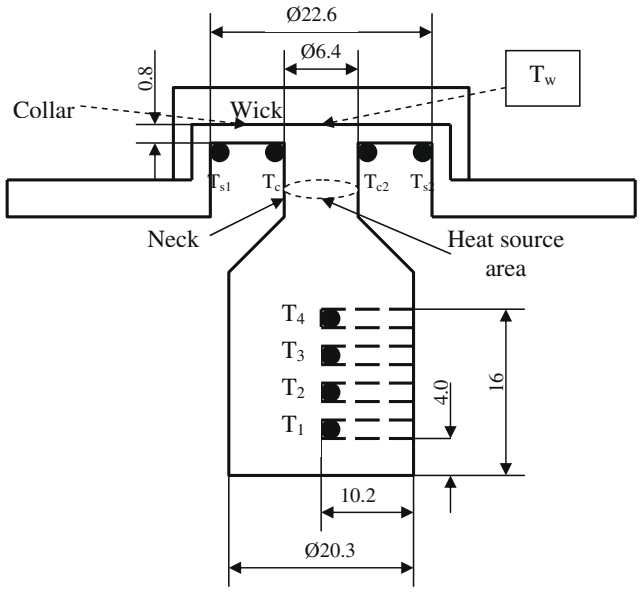

Fig. 2. Copper base with a wick (all measures are in mm).

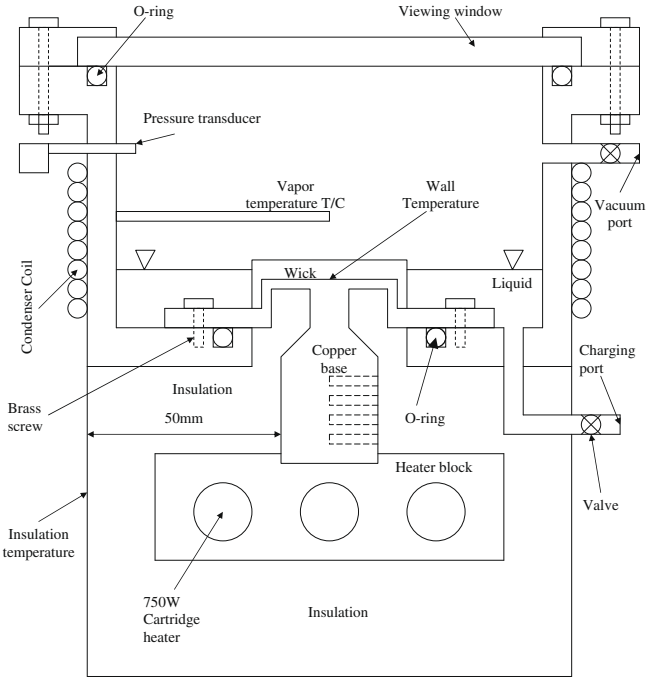

Fig. 3. Test rig for testing wicks.

The heater block had a 3 mm deep hole with diameter 20.5 mm to facilitate soldering of the heater to the copper base.

Twelve calibrated thermocouples (K-type, 36AWG, PFA insulation) were carefully glued with a high temperature resistant metal filled epoxy adhesive at locations T_1, T_2, T_3, T_4, T_{c1}, T_{s1}, T_{c2}, T_{s2}, T_{c3}, T_{s3}, T_{c4}, and T_{s4}. In Fig. 2, a plane that goes through T_{s3}, T_{s4}, T_{c3}, T_{c4} is perpendicular to a plane that goes through T_{c1}, T_{s1}, T_{c2}, T_{s2} and is therefore not shown. A K-type Inconel 600 sheathed thermocouple, 1.6 mm diameter, was placed inside the test rig, approximately 10 mm above the wick to monitor saturation temperature. A pressure transducer was inserted into the test rig to measure saturation pressure inside the test rig.

Once all thermocouples were in place, the test rig was sealed with a viewing window on the top and evacuated. The wick was saturated with distilled water through a charging port of the test rig. The heater was soldered to the copper base and electrically ground. Both the copper base and the heater were insulated with an amorphous silica blanket (thermal conductivity 0.05 W/m K at 250 °C). The thickness of the insulation around copper base was 50 mm. A condenser with a cooling coil was located on the body of the test rig. Water, at a constant temperature 40 ± 0.25 °C, was circulated through the cooling coil.

The heater was turned on and set to a medium high heat flux and let run for approximately 10 min. Next, the vacuum pump (Alcatel SD2005 two stage rotary vane vacuum pump) was run for approximately 10 min to reach a vapor pressure of 6773 Pa (0.068 bar). This way most of the non-condensable gases from the wick and the test rig were removed. Water level was adjusted right below the top of the wick (see Fig. 3). The power to the heater was turned off and the wick was allowed to cool down and to fully saturate for 6 h. After 6 h the stepper motor controlled power supply was turned on and the heat being supplied to the heater was gradually increased. Temperature readings were taken at several steady states with a Personal Daq/56 USB Data Acquisition System from IOtech Inc. Steady state was reached in 20 min and temperatures were recorded for 5 min for each steady state heat flux. It took total of 13 h to test one wick.

Once all data were taken, 50 temperature readings were averaged for each steady state. Steady state was assumed when the temperature did not rise for more than 0.5 °C in 5 min. A linear regression on temperatures T_1 to T_4 was made and temperature gradients for all heat fluxes were found. Knowing temperature gradients inside copper bases and temperatures of the copper collars at locations T_c, and T_s, the net heat flux going into the evaporator wick was calculated as:

$$q = \frac{1}{A_{neck}}(Q_{total} - Q_{radial} - Q_{loss}) \tag{1}$$

Since the thickness of the collar was only 0. 8 mm, we assumed that the temperatures measured underneath the copper collar were equal to the temperatures in the middle of the copper collar thickness (0.4 mm underneath the wick). Temperature of the insulation, T_{ins}, increased from 25 to 40 °C as the temperature of the copper base got increased. By assuming one-dimensional Fourier's law of heat conduction and dimensions from Fig. 2, the net heat flux in the evaporator, was determined from

$$Q = k(T_{ave}) \cdot \frac{dT}{dx} \cdot \left(\frac{\pi \cdot 0.0203^2}{4}\right) - \frac{2\pi k(T'_{ave}) \cdot 0.008 \cdot (T_c - T_s)}{\ln\left(\frac{22.6}{6.4}\right)} - \frac{2\pi k(T''_{ave}) \cdot 0.03 \cdot (T_{ave} - T_{ins})}{\ln\left(\frac{60.2}{10.2}\right)}$$

$$q = \frac{Q}{\left(\frac{\pi \cdot 0.064^2}{4}\right)} \tag{2}$$

where $k(T_{ave})$ is thermal conductivity of copper base, $k(T'_{ave})$ is thermal conductivity of copper collar, and $k(T''_{ave})$ is thermal conductivity of the insulation. The thickness of the insulation was 50 mm for all the cases. To account for uncertainties in attaching thermocouples underneath the copper collar, eight thermocouples were used. For each pair of T_c and T_s one radial heat flux was calculated. From the four radial heat fluxes an average radial heat flux, with its corresponding uncertainty, was computed. Knowing temperatures in copper base and the net heat flux into the evaporator, the wall temperature, T_w, was calculated. The wall temperature was defined as the interface temperature between the wick and the copper base

(Fig. 2). Once wall temperatures and heat fluxes were obtained, the wick resistances, R_{wick}, were computed from:

$$R_{wick} = \frac{(T_w - T_{sat})}{q} \quad (3)$$

T_{sat} is saturation temperature and it was measured with a thermocouple located above the wick. T_{sat} was also obtained from steam tables using measured vapor pressure The radial heat flux into the wick above the copper collar was neglected since the product of thermal conductivity of the wick times thickness of the wick was at least 10-times smaller than a product of thermal conductivity of the copper times thickness of the collar. Thermal conductivity of the copper was taken to be 401 W/m K at 300 K and 393 W/m K at 400 K, and thermal conductivity of biporous wicks 4–22 W/m K (see Table 1).

4. Experimental results and discussion of the results

First, thermophysical properties for all biporous wicks were measured. Second, three monoporous and 15 biporous wicks with different cluster/particle diameters and wick thickness were tested. Third, one biporous wick was sintered into four different wick thicknesses and tested at different heat fluxes.

Table 1 summarizes cluster porosities, ε, wick porosities, ε_w, maximum capillary pressure of clusters (also known as bubble point pressure), Δp_{max}, liquid permeability of clusters, K_l, vapor permeability of the wicks, K_v, thermal conductivity of clusters, k_c, and thermal conductivity of the wicks, k_w. Details about the thermophysical properties testing methods can be found in Semenic et al. [12]. The first number in Table 1 is average cluster diameter, the second number is average particle diameter, and, the third number is the wick thickness. The results of Table 1 show that porosity of biporous wicks does not depend on cluster and particle size. Liquid and vapor permeabilities increase with pore (particle/cluster) size while capillary pressure decreases with pore (particle) size. Thermal conductivities of the particles/clusters seem to be only a function of porosity and not the size of the clusters/particles. Fig. 4 shows heat flux vs. superheat, $T_w - T_{sat}$, for three monoporous wicks. The first number in the legend represents particle diameter and the second number the wick thickness. The Fig. 4 shows that the best performs 107/500 wick. Unfortunately, all three monoporous wicks dried out above 250–300 W/cm^2. We can also see that the pressure inside the test chamber increased with the heat flux from 0.06 to 0.1 bar. Above 300 W/cm^2, the vapor temperature measured with the thermocouple was higher than the saturation temperature calculated from saturation pressure. This indicates that the vapor state above 300 W/cm^2 was superheated vapor. Average uncertainties in measuring heat fluxes were less than ±20%. The primary source of errors was thermocouple contact resistance and the secondary source, the displacement error of thermocouples T_c and T_s.

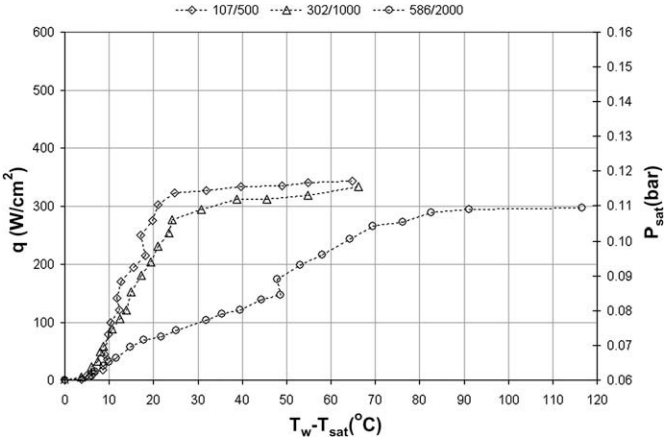

Fig. 4. Heat flux vs. superheat for monoporous wicks.

Figs. 5–7 show heat fluxes vs. superheats for 15 biporous wicks. The first number in the legends represents average cluster diameter, the second number, the average particle diameter, and the third number, the wick thickness. By comparing a monoporous wick 302/1000 from Fig. 4 with any of the biporous wicks on the Fig. 5, we can see that biporous wicks can handle heat fluxes above 300 W/cm^2. We can define a critical heat flux (CHF) of a monoporous or a biporous wick as the heat flux with a minimum wick thermal resistance, R_w. For example, the CHF for the 302/1000 wick is 280 W/cm^2 (R_w = 0.09 °C/W/cm^2) while the CHF for the biporous wick 302/58/1000 in Fig. 5 is 293 W/cm^2 (R_w = 0.126 °C/W/cm^2). Fig. 5 also shows that, the same wick 302/58/1000 still operates at 513 W/cm^2 (R_w = 0.132 °C/W/cm^2) and a superheat of 67 °C.

High critical superheats of biporous wicks indicate that at CHF a part of the biporous wick is already in film boiling regime. By comparing measured vapor temperature with calculated vapor temperature from the measured pressure, we could see that the vapor state above the wick is still saturated vapor; however, the vapor inside the wick is most probably superheated. Table 2 lists CHFs for

Table 1
Thermophysical properties for biporous wicks.

D (μm)	d (μm)	t (μm)	ε	ε_w	Δp_{max} (Pa)	K_l (m^2)	K_v (m^2)	k_c at 42 °C (W/m K)	k_w at 86 °C (W/m K)
302	41	1000	0.36	0.67	–	3.00 E−13	2.0 E−10	145	–
586	41	2000		0.68			5.2 E−10		6
892	41	3000		0.67			8.7 E−10		4
302	58	1000	0.27	0.63	16,299	1.50 E−12	1.8 E−10	146	15
586	58	2000		0.66			5.1 E−10		8
892	58	3000		0.66			9.3 E−10		7
302	72	1000	0.29	0.61	12,193	1.60 E−12	1.7 E−10	147	22
586	72	2000		0.65			5.0 E−10		10
892	72	3000		0.63			8.4 E−10		8
302	74	1000	0.28	0.63	15,179	1.50 E−12	1.9 E−10	139	21
586	74	2000		0.65			5.4 E−10		10
892	74	3000		0.65			9.2 E−10		9
302	83	1000	0.28	0.51	11,571	2.40 E−12	1.3 E−10	132	16
586	83	2000		0.64			4.5 E−10		9
892	83	3000		0.64			8.4 E−10		6
455	63	800	–	–	15,428	1.58 E−12	–	–	–
455	63	1400		–			–		–
455	63	2000		–			–		–
455	63	3000		–			–		–

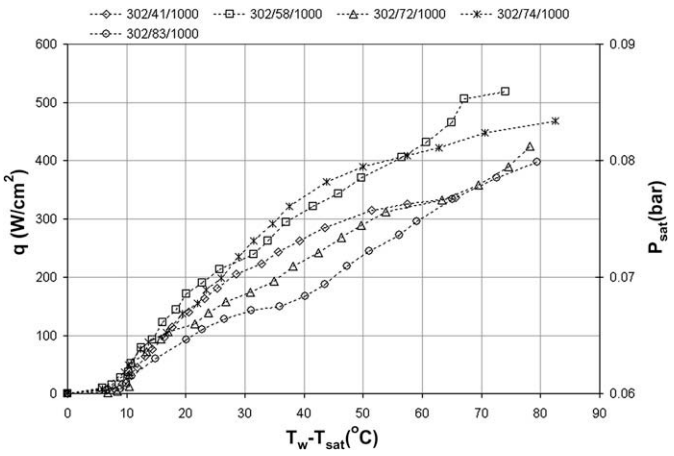

Fig. 5. Heat flux vs. superheat for biporous wicks with average cluster diameter 302 μm.

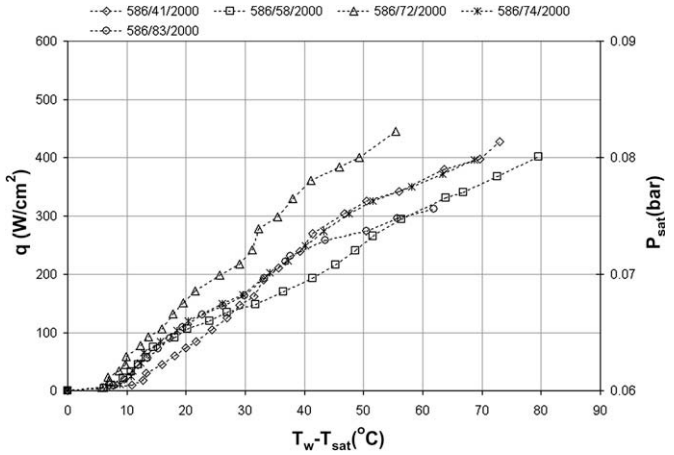

Fig. 6. Heat flux vs. superheat for biporous wicks with average cluster diameter 586 μm.

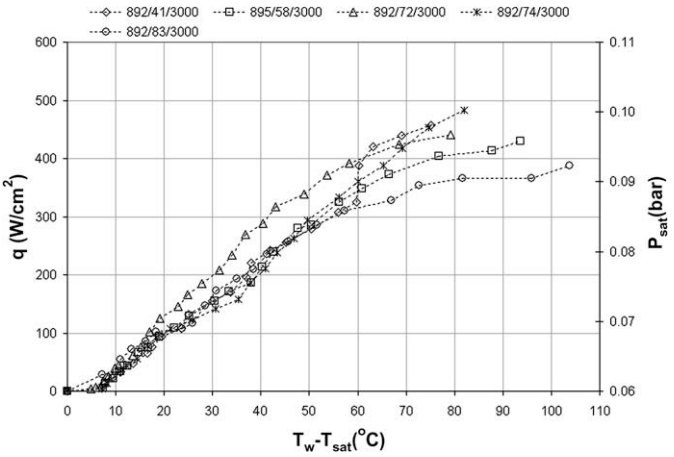

Fig. 7. Heat flux vs. superheat for biporous wicks with average cluster diameter 892 μm.

all the biporous wicks tested. The highest CHF among the first 15 biporous wicks was measured for the 892/74/3000 biporous wick (CHF = 454 W/cm^2, R_w = 0.164 °C/W/cm^2).

Table 2
CHF, critical superheat, and critical wick thermal resistance for biporous wicks.

D (μm)	d (μm)	t (μm)	CHF (W/cm^2)	ΔT_{CHF} (°C)	$R_{wick,CHF}$ (°C/W/cm^2)
302	41	1000	244	36	0.146
586	41	2000	304	47	0.154
892	41	3000	420	63	0.150
302	58	1000	293	37	0.126
586	58	2000	293	56	0.192
892	58	3000	325	56	0.172
302	72	1000	311	54	0.173
586	72	2000	360	41	0.114
892	72	3000	316	43	0.136
302	74	1000	321	38	0.117
586	74	2000	303	48	0.157
892	74	3000	454	75	0.164
302	83	1000	334	65	0.195
586	83	2000	232	38	0.163
892	83	3000	236	41	0.175
455	63	800	523	49	0.095
455	63	1400	428	53	0.125
455	63	2000	589	100	0.171
455	63	3000	990	147	0.148

Data in Table 2 were used in an optimization algorithm to look for biporous wick geometrical parameters (cluster diameter, particle diameter, and wick thickness) that yield minimum wick resistance and maximum CHF. No clear relationship was found. Following, heat fluxes at constant wall temperature were interpolated from data in Figs. 5–7 and used to develop a correlation between wick geometrical parameters and the heat fluxes. For example at the wall temperature of 90 °C, the most optimal biporous wick had the geometrical parameters: 400 μm < D < 600 μm, 60 μm < d < 70 μm, and 1000 μm < t < 2000 μm (Fig. 8).

Following the trend in Fig. 8, four biporous wicks with average cluster diameter 455 μm and average particle diameter 63 μm were sintered into four different thicknesses and tested. Fig. 9 shows that 455/63/800 wick performs better than the rest of the wicks for heat fluxes below 600 W/cm^2. Table 2 shows that the CHF for this wick is 523 W/cm^2. Fig. 9 also shows that 455/63/2000 and 455/63/3000 wicks still operate at very high superheats ~140 °C. This is most probably because the radial heat conduction into the wick at very high heat fluxes and superheats can no longer be neglected and results in radial spreading of the evaporation front into the wick. However, if the application allows heat spreading into the wick then thick biporous wicks can be used for heat fluxes as high as 700–1000 W/cm^2.

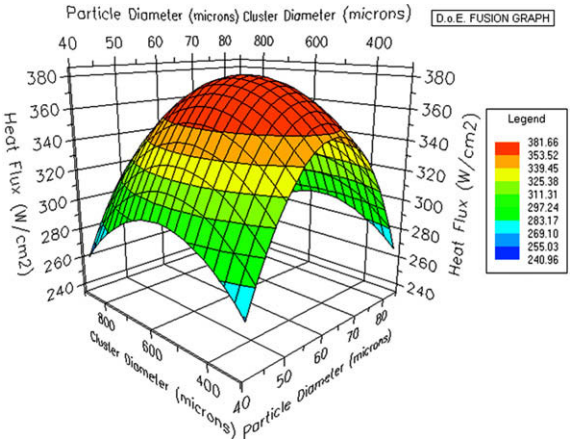

Fig. 8. Heat fluxes at 90 °C wall temperature for different cluster and particle diameters.

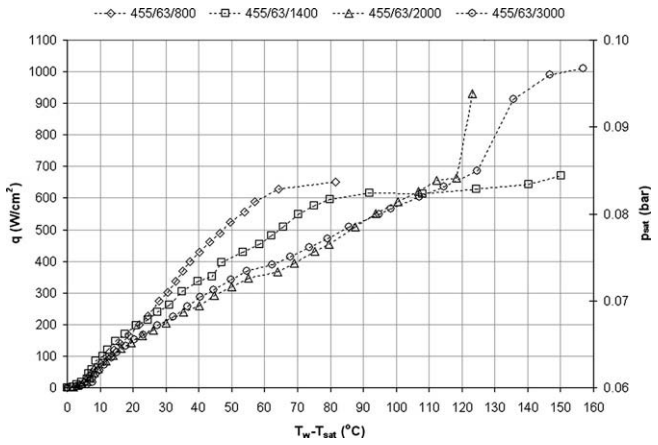

Fig. 9. Heat flux vs. superheat for a biporous wick with different wick thickness.

Fig. 10 shows a comparison of heat fluxes at different superheats for a thin monoporous wick and a thin biporous wick. There are three characteristic points on each of the curves in Fig. 10. The first point is where the gradient on the curve starts to increase, the second point is where the wick resistance is minimal (defined as CHF) and the third point is the beginning of dryout. For monoporous wicks, the first point could physically represent the increase of the evaporating menisci. As the heat flux increases above ~20 W/cm^2, the menisci profiles start to vary and the contact angle of the menisci starts to decrease resulting in an increase of the evaporating thin film regions. As the heat flux approaches CHF at the second point, the contact angle reaches its minimum and the evaporating menisci start to recede. The area of the evaporating thin film regions starts to decrease rapidly. The third point (beginning of dryout), is determined either by a capillary or a boiling limit of the wick.

In a thin biporous wick, the evaporating interface consists of evaporating menisci of large pores and evaporating menisci of small pores. The first point in thin biporous wicks could physically mean the heat flux where the contact angle of large menisci starts to decrease and the evaporating menisci of large pores start to increase. As the heat flux increases, the contact angle of large pores reaches a minimum and the menisci of large pores start to recede. When the menisci in large pores start to recede, the number of menisci in small pores starts to increase. This could explain why the CHF for a thin biporous wick is at higher heat flux than the CHF for a monoporous wick. It is expected that at point two, the large pores are completely clear of liquid and the maximum number of small pores become active. Overall heat transfer coefficient for a thin biporous wick is proportional to a number of evaporating menisci meaning that it reaches its maximum when the number of the evaporating menisci is the highest. This is the case at the CHF. After passing the point two or the CHF, the small pores menisci start to recede into the pores. Dryout of a thin biporous wick is determined by boiling or capillary limit of small pores.

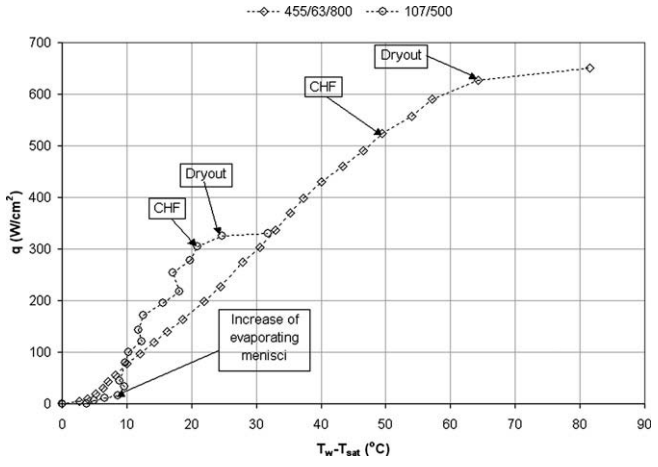

Fig. 10. Heat flux vs. superheat for a monoporous wick and a thin biporous wick.

Heat transfer mechanism for thick biporous wicks is more complex than for thin biporous wicks. During the test of thick biporous wicks it was visually confirmed that at medium high-to-high heat fluxes, there exist vapor columns between the clusters (boiling stage of a thick biporous wick). Large pores on top of the 455/63/2000 and 455/63/3000 (Fig. 9) biporous wicks (thick biporous wicks) that did not develop vapor columns were filled with working fluid throughout the entire test (up to 1 kW/cm^2). Very high superheats at heat fluxes above 600 W/cm^2 indicate that the center of the wick above the heated surface was already in film boiling regime (vapor blanket formation stage), however, the top of the wick was still saturated. This means that the heat conducted from the heated surface through the film-boiling region to the liquid–vapor interface inside the wick. The vapor was produced at evaporating menisci of small pores and the vapor columns developed between some of the large pores and ducted the vapor to the top surface of the wick. Smaller pores between clusters were more likely to remain filled with liquid and to supply liquid to clusters around larger pores filled with vapor columns. As the heat flux approached 1 kW/cm^2, the vapor blanket started to spread from the center of the wick to the entire wick. The second evaporation stage with almost isothermal heat flux increase reported in [11] was not seen. The heat flux increase from 600 to 900 W/cm^2 at relatively low temperature difference increase for the 455/63/2000 and 455/63/3000 wicks is more likely to appear due to radial conduction into the wick and three dimensional spreading of the evaporation front into the wick.

5. Uncertainty analysis

Temperatures were measured using a Personal Daq/56 with PDQ2 extension mode data acquisition instrumentation and a 22-bit A/D converter. The unit has built in cold-junction-compensation with an accuracy of ±0.5 °C [13]. The acquired voltage was automatically converted into compensated linearized temperature readings. Temperatures were measured with K-type thermocouples at a sampling rate of 0.19 Hz and averaged over 310 ms intervals. IOtech Inc. [13] specify the accuracy in measuring temperature at 0 °C at 310 ms intervals to be at least ±0.4 °C.

Mills and Chang [14] define the precision uncertainty, P, as the magnitude of the error that will yield a 95% confidence that the true value, a_{true}, of a measurement a_i lies within the interval $a_i \pm P$. Assuming a normal population, we can obtain the population mean, μ, a best approximation of the a_{true}, using the following relationship:

$$\mu = \bar{a} \pm t_{\nu,\%} S_{\bar{a}}, \tag{4}$$

where $\bar{a}$ is the mean of a sample with sample size N, calculated using

$$\bar{a} = \frac{1}{N}\sum_{i=1}^{N} a_i \tag{5}$$

Here $S_{\bar{a}}$ is the standard deviation of the sample mean obtained from

$$S_{\bar{a}} = \frac{S_a}{\sqrt{N}} = \frac{1}{\sqrt{N}}\left[\frac{1}{N-1}\sum_{i=1}^{N}(a_i - \bar{a})^2\right]^{1/2} \tag{6}$$

where $t_{v,\%}$ is the Student's t-distribution variable. The quantity S_a in Eq. (7) is the sample standard deviation. The variable t depends on the degrees of freedom, $v = (N - 1)$, and the confidence level, %. t_{95} values for different degrees of freedom are tabulated in the literature, for example [14].

Precision uncertainty for a sample of 31 points in measuring ice and boiling water was measured ±0.03 °C and ±0.04 °C, respectively. To demonstrate how the precision error affected the heat flux measurements, the actual data for the 586/72/2000 biporous wick at a heat flux of 300 W/cm^2 were used. For example precision error of temperature T_1 at this heat flux for 50 temperature readings is ±0.08 °C. By taking the worst possible scenario, where temperatures T_1 and T_4 are replaced with $(T_1 - 0.08\,^\circ\text{C})$ and $(T_4 + 0.08\,^\circ\text{C})$, the resulting heat flux is 296 W/cm^2, which is at most 1% lower.

Total bias uncertainties will be divided into bias uncertainties in calculating the neck heat flux, B_{neck} and bias uncertainties in calculating radial heat flux, B_{rad}.

By knowing the positions of thermocouples, x_i, and temperature T_i at location x_i, we can perform a least squares curve fit and obtain a linear correlation:

$$\zeta_i = \left(\frac{dT}{dx}\right)x + c \tag{7}$$

We can define a standard error for the curve-fit as:

$$S_{\text{T}} = \sqrt{\frac{1}{N-2}\sum_{i=1}^{N}(T_i - \zeta_i)^2} \tag{8}$$

and calculate a standard error in the temperature gradient, S_{neck}, as:

$$S_{\text{neck}} = \left(\frac{S_{\text{T}}^2}{S_x}\right)^{1/2} \tag{9}$$

where S_x is given as:

$$S_x = \sum_{i=1}^{N} x_i^2 - \frac{1}{N}\left(\sum_{i=1}^{N} x_i\right)^2 \tag{10}$$

The corresponding bias uncertainty in calculating the neck heat flux, B_{neck}, is:

$$B_{\text{neck}} = t_{v,\%} S_{\text{neck}} \tag{11}$$

where $t_{v,\%}$ is the Student's t-distribution variable with $v = N - 2$. The bias uncertainty in q_{neck} is calculated for all wicks and heat fluxes using Eqs. (8)–(12).Bias uncertainties in calculating radial heat flux, B_{rad}, is calculated as:

$$B_{\text{rad}} = t_{v,\%} S_{\text{rad,ave}} \tag{12}$$

where $S_{\text{rad,ave}}$ is the standard deviation of the mean of the radial heat flux calculated from

$$S_{\text{rad,ave}} = \frac{1}{\sqrt{N}}\left[\frac{1}{N-1}\sum_{i=1}^{N}\left(q_{\text{rad},i} - q_{\text{rad,ave}}\right)^2\right]^{1/2} \tag{13}$$

where $q_{\text{rad,ave}}$ is the average radial heat flux and $q_{\text{rad},i}$, the ith radial heat flux calculated from the ith pair of (T_c, T_s). The total bias uncertainty, B, is calculated as the sum of both bias uncertainties, $B = B_{\text{neck}} + B_{\text{rad}}$. The total uncertainty in measuring the heat flux is defined as

$$U = \sqrt{B^2 + P^2} \tag{14}$$

The average relative uncertainty, defined as $U_i/q_i{}^* 100$, for heat fluxes, q_i, and corresponding uncertainties, U_i, from Table 2, is ±15%. Uncertainties in our data neglect precision uncertainty, since $B >> P$.

Besides uncertainties in heat flux, there is also uncertainty in the wall temperature, which is calculated in the same manner as B_{neck}. Average uncertainty in T_{w} at 90 °C is 8 °C with a minimum of 2 °C for the 302/41/1000 wick and a maximum 16 °C for the 892/74/3000 wick.

In general, precision uncertainty does not depend on a heat flux, while q_{rad} becomes worst at high heat flux. On the other hand, q_{neck} and T_{w}, have higher uncertainties at low heat fluxes and lower uncertainties at high heat fluxes.

The uncertainties in calculating q_{neck} and T_{w} could be reduced by making a copper base longer than 20 mm and by measuring the temperature gradients inside the copper base with more than four thermocouples. Uncertainties in measuring radial heat fluxes could be reduced by placing more than eight thermocouples underneath the copper collar.

6. Concluding remarks

This work tested 19 biporous wicks and three monoporous wicks. Monoporous wicks are wicks with one characteristic pore size while biporous wicks are wicks with two characteristic pore sizes. Thermophysical properties (capillary pressure of clusters, liquid permeability of clusters, vapor permeability of the wicks, thermal conductivity of clusters, and thermal conductivity of the wicks) were measured for the biporous wicks. Wicks were tested at different heat fluxes using degassed distilled water. The best monoporous wick tested had CHF at 300 W/cm^2 (21 °C superheat), the best thin biporous wick tested had CHF at 520 W/cm^2 (50 °C superheat), and the best thick biporous wick tested had CHF at 990 W/cm^2 (147 °C superheat). Thin biporous wicks were distinguished from thick biporous wicks by using a criteria of [11] where thin biporous wicks are defined as wicks that are thin enough so that the bubble nucleation does not occur inside the wick and the menisci recede into the large pores of the wicks. A thick biporous wicks, on the other hand, are wicks where bubbles start to form inside the wicks and to form vapor jets.

Monoporous wicks and thin biporous wicks were found to remove heat through evaporation from liquid–vapor menisci. Thin biporous wicks can reach higher CHF than monoporous wicks because they have active evaporating menisci not only on top surface of the wick but also inside the wick. Thick biporous wicks can reach even higher CHF than thin biporous wicks, because at very high heat fluxes even though the center of the wick above the heated surface is in film boiling regime (vapor blanket formation above the heated surface), the top layer of the wick continues to supply liquid to the evaporating menisci inside the wick above the vapor blanket. Also at high heat fluxes, the heat spreads from the heated surface radially into the wick increasing the area of the evaporation front inside the wick. Thick biporous wicks can be used for 600–1000 W/cm^2 applications where high superheats and heat spreading into the wick are acceptable. For applications below 600 W/cm^2 are recommended thin biporous wicks and for applications below 300 W/cm^2 are recommended monoporous wicks.

Acknowledgements

The authors acknowledge the support of U.S. Navy/Office of Naval Research and Dr. Mark Spector as program manager. The grant award number is N00014-04-1-0280.

References

[1] P.A. Vityaz, S.K. Konev, V.B. Medvedev, V.K. Sheleg, Heat pipes with bidispersed capillary structures, in: Proc. 5th International Heat Pipe Conference, vol. 1, 1984, pp. 127–135.
[2] S.V. Konev, F. Polasek, L. Horvat, Investigation of boiling in capillary structures, Heat Transfer-Sov. Res. 19 (1) (1987) 14–17.

[3] X.L. Cao, P. Cheng, T.S. Zhao, Experimental study of evaporative heat transfer in sintered copper bidispersed wick structures, J. Thermophys. Heat Transfer 16 (4) (2002) 547–552.
[4] T. Semenic, Y.Y. Lin, I. Catton, Use of liquid film evaporation in biporous media to achieve high heat flux over large areas, in: Proc. Summer Heat Transfer Conference, San Francisco, CA, July 17–22, 2005.
[5] M.T. North, J.H. Rosenfeld, R.M. Shaubach, Liquid film evaporation from bidisperse capillary wicks in heat pipe evaporators, in: Proc. 9th International Heat Pipe Conference, Albuquerque, NM, May 1–5, 1995.
[6] J.H. Rosenfeld, M.T. North, Porous media heat exchanger for cooling of high-power optical components, Opt. Eng. 34 (2/335) (1995).
[7] E. Merilo, T. Semenic, I. Catton, Experimental investigation of boiling heat transfer in bidispersed media, in: Proc. 13th International Heat Pipe Conference, Shanghai, China, September 21–25, 2004.
[8] T. Semenic, Y.Y. Lin, I. Catton, D.B. Sarraf, Use of biporous wicks to remove high heat fluxes, Appl. Thermal Eng. 28 (2008) 278–283.
[9] M.T. North, Personal communication, 2000.
[10] M.A. Hanlon, H.B. Ma, Evaporation heat transfer in sintered porous media, ASME J. Heat Transfer 125 (2003) 644–652.
[11] J. Wang, I. Catton, Vaporization heat transfer in biporous wicks of heat pipe evaporators, in: Proc. 13th International Heat Pipe Conference, Shanghai, China, September 21–25, 2004.
[12] T. Semenic, Y.Y. Lin, I. Catton, Thermophysical properties of biporous heat pipe evaporators, ASME J. Heat Transfer 130 (2008) 022602-1–022602-10.
[13] IOtech Inc., Personal Daq User's Manual, p/n 491-0901, Rev. 5.0, 2003.
[14] A.F. Mills, B.H. Chang, Error Analysis of Experiments, A Manual for Engineering Students, unpublished, 2003.